ACS OMEGA

http://pubs.acs.org/journal/acsodf

Article

A Genetic Algorithm for Universal Optimization of Ultrasensitive Surface Plasmon Resonance Sensors with 2D Materials

Matej Sebek,* Nguyen Thi Kim Thanh, Xiaodi Su, and Jinghua Teng*

Cite This: *ACS Omega* 2023, 8, 20792−20800

Read Online

ACCESS | Metrics & More | Article Recommendations | Supporting Information

ABSTRACT: We present a general optimization technique for surface plasmon resonance, (SPR) yielding a range of ultrasensitive SPR sensors from a materials database with an enhancement of ∼100%. Applying the algorithm, we propose and demonstrate a novel dual-mode SPR structure coupling SPP and a waveguide mode within GeO_2 featuring an anticrossing behavior and an unprecedented sensitivity of 1364 deg/RIU. An SPR sensor operating at wavelengths of 633 nm having a bimetal Al/Ag structure sandwiched between hBN can achieve a sensitivity of 578 deg/RIU. For a wavelength of 785 nm, we optimized a sensor as a Ag layer sandwiched between hBN/MoS_2/hBN heterostructures achieving a sensitivity of 676 deg/RIU. Our work provides a guideline and general technique for the design and optimization of high sensitivity SPR sensors for various sensing applications in the future.

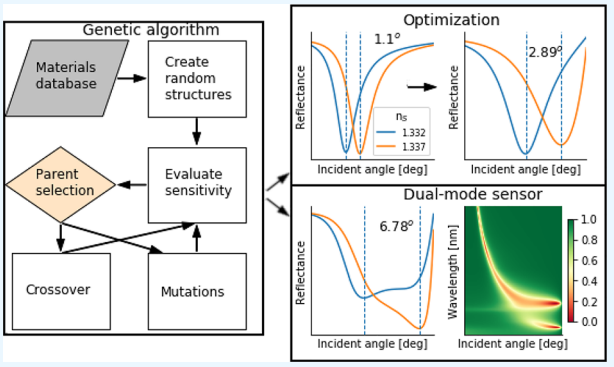

INTRODUCTION

Plasmon resonances in noble metals and other metallic and semimetallic materials[1,2] find use in applications ranging from imaging[3] to photodynamic therapy,[4] sensing,[5] lasing,[6] and color generation.[7] Surface plasmon resonance (SPR) sensors with thin metal films supporting surface plasmon polaritons (SPP),[8] an evanescent wave excited on the interface between a metal film and a dielectric superstrate, are commonly used for label-free detection of a variety of analytes ranging from gases[9] to the SARS-CoV-2 virus.[10] The metal surface is typically biofunctionalized to selectively capture the target analyte. The binding of the analyte leads to a change of the refractive index of the superstrate yielding a change in the plasmon wavelength or the resonant angle, phase, or polarization of the optical wave. The precise measurement of these signals leads to the quantification of the target analytes.[11]

There have been numerous efforts to increase the sensitivity of SPR sensors by using 2D materials,[1] guided waves,[12] gratings,[13] nanoparticles,[14] fabricated nanostructures,[15] or thin dielectric layers.[16] Due to the layered nature, van der Waals (vdW) materials are highly desired for the improvement of SPR sensor performance as they allow the tuning of the refractive index down to one atomic layer and can improve the adsorption of biomolecules.[17−20] This approach has been proposed for phase-sensitive SPR sensors as well.[21] Previously, our group predicted that an SPR sensor based on graphene and MoS_2 has an ultrahigh sensitivity of 536 deg/refractive index unit (RIU).[22]

Genetic algorithms are convenient for the optimization of photonic structures due to their simplicity and reasonable computation times.[23] Examples of photonic structures that can be optimized and engineered in this way include photonic crystals[24,25] and photonic crystal fibers,[26] plasmonic arrays,[27] plasmonic color filters,[28] metaoptics, and metasurfaces.[29,30] In the case of SPR sensors, a genetic algorithm has been only used to optimize specific cases and structures such as guided-wave,[31,32] magneto-optic SPR,[33] Au−Ag-dielectric-graphene,[34] transition metal dichalcogenide (TMDC)/graphene,[35] and Au nanostructure.[36]

Here, we propose a genetic algorithm to significantly generalize the optimization of SPR sensors in the Kretschmann configuration (SPP is excited through a prism on top of which the metal film is deposited).[37] We apply the algorithm and show three different cases as examples of sensors with high sensitivity. We propose and discuss a novel architecture featuring two plasmonic resonances and exploiting coupling between them when the refractive index of the sensing layer changes. We also demonstrate the applicability of the algorithm both for visible and near-infrared wavelengths in the optimization of standard single-mode SPR sensors.

Received: March 1, 2023
Accepted: May 9, 2023
Published: May 26, 2023

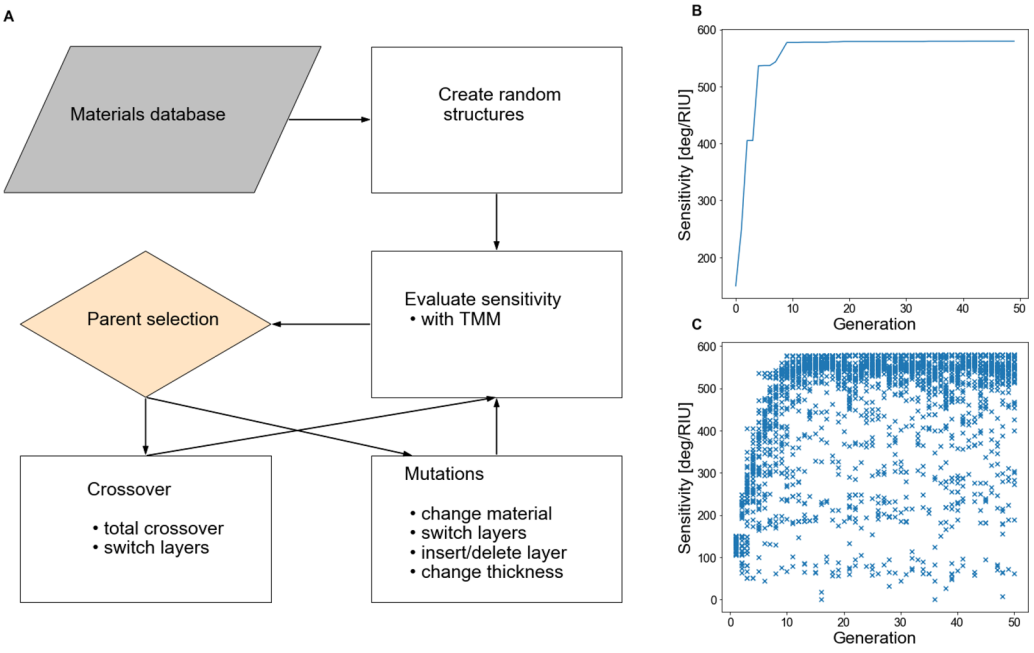

Figure 1. (A) Scheme of the genetic algorithm. The materials database is loaded, and a pool of random structures is generated. Fitness is then evaluated by calculating the sensitivity of each structure with a transfer matrix method. Parents are selected with a weighted wheel, and modifications are applied either as mutations or crossovers. (B) Evolution of the sensitivity of the best-generated sensors. (C) Scatter plot of sensitivities of the whole population.

RESULTS

The Genetic Algorithm. Our genetic optimization is based on a quasi-random generation of a number of multilayer sequences followed by an evaluation of the plasmon resonance shift by a fixed change of the refractive index of the environment with a transfer matrix method, selection of parents for the next generation, and random mutations of several types.

The flowchart of the algorithm is shown in Figure 1A. For the initial population, we have created each structure with a random number of layers of random materials including metals, dielectrics, and 2D materials. The refractive indices of materials are loaded from the database of refractive indices.[38] The thickness is encoded discretely either using layer thickness for layered materials or 1 nm steps for nonlayered materials. The list of refractive indices and thickness steps for materials used for the structures mentioned in this study can be found in Table S1.

For the initial population, the maximum number of non-2D dielectric layers is set to 3, the maximum number of commonly used plasmonic metal layers (by which we mean Ag, Au, and Al) to 3, the maximum number of 2D materials (see Table S1) is 4, and the maximum number of nonplasmonic metals is 1. The size of the population is set to 50, which is a good compromise between speed of the algorithm and diversity of the population and is in accordance with previous studies on genetic algorithms.[39] When more layers are allowed, the proportion of architectures without plasmonic resonance is too high and the algorithm does not converge in a reasonable time. However, due to the mutations (i.e., adding another layer), the number of materials can gradually increase later. Another consideration is that the proposed structures shall be reasonably simple to fabricate. Boundaries are also set for the thickness of the layers. For non-2D materials, the minimum thickness is set to 5 nm and a maximum thickness to 100 nm. For 2D materials, the minimum thickness is one layer and the maximum thickness is 50 layers. The thicknesses of 2D materials used in this study are compiled in Table S1.

The objective function of the algorithm is defined by the sensitivity of the SPR sensor as $S = {}^{\Delta\sigma}/_{\Delta n_s}$, where $\Delta\theta$ is the change of the resonance angle and Δn_s is the change of the refractive index of the sensing environment. Such as in previous studies,[22] the resonant angle is calculated using a transfer matrix method, with the zeroth layer being the incident medium with the refractive index of the prism, n layers of the sensor being the stratified medium, and the $(n + 1)$-th layer being the sensing medium with the initial refractive index $n_s = 1.332$ and $n_s = 1.337$ after the analyte adsorption. The $n_s = 1.332$ is chosen as an example of a liquid matrix (water) and increases with the concentration of the analyte, which has a typically higher refractive index than that of the solvent.

Since the accuracy of the calculated sensitivity depends on the refinement of the spacing between two frequency points, we employ a two-step calculation to achieve a good compromise between the speed of the algorithm and the accuracy of the calculation. First, the angular reflectance, the position of the plasmonic resonance, and the full width at half-maximum (fwhm) of the spectrum is roughly calculated with a spacing of 0.1°. The precise position of the plasmonic resonance is then recalculated in the range of the fwhm around the original position. Since the dip is not always symmetric, the fwhm is split into two halves independent of each other.

The algorithm uses overlapping generations. 10% of each generation with the highest sensitivity automatically progresses to the next generation. The rest of the next generation is reserved for parents selected from the original generation with a probability—weighted by the sensitivities of particular structures—the so-called weighted wheel.

https://doi.org/10.1021/acsomega.3c01387
ACS Omega 2023, 8, 20792−20800

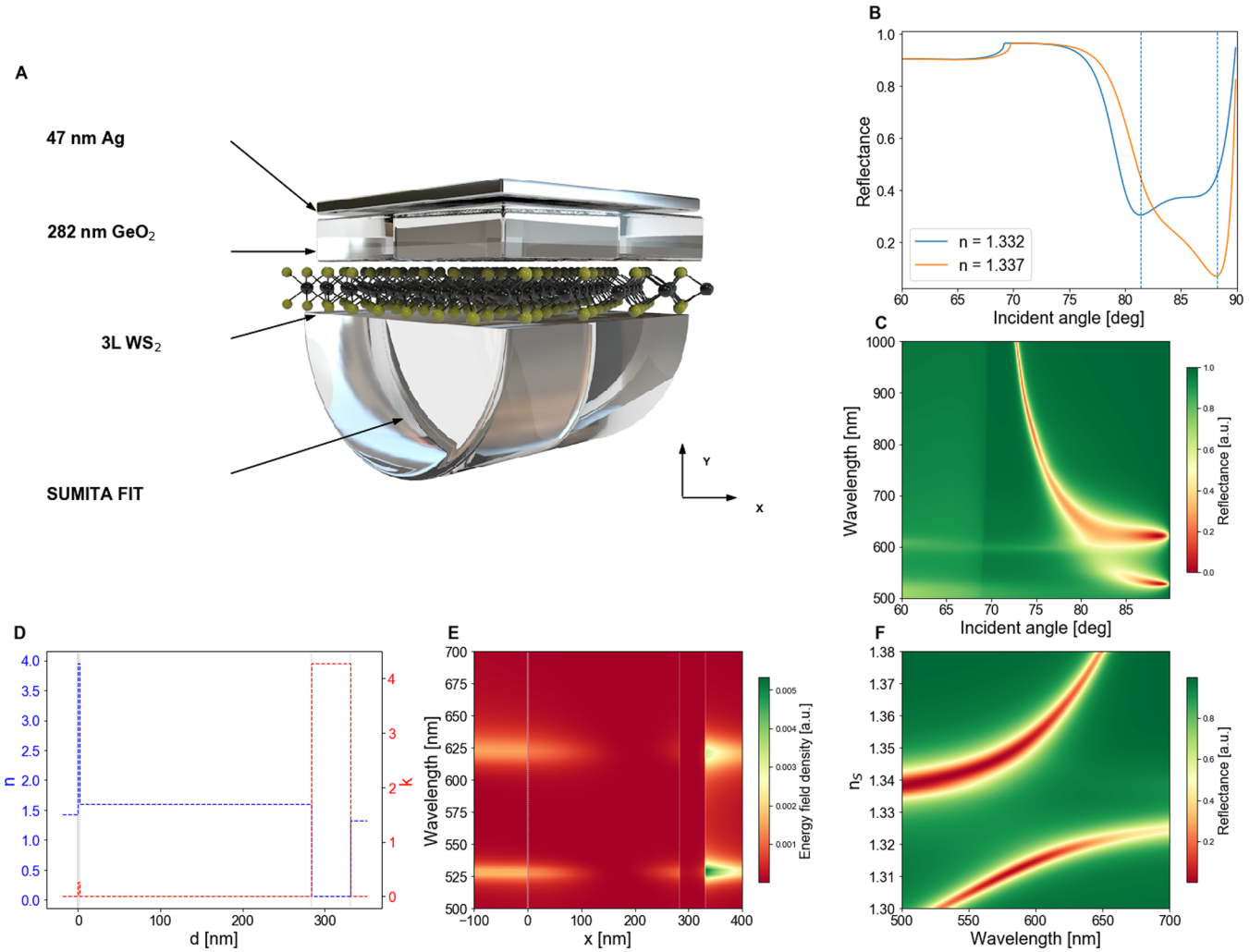

Figure 2. (A) Scheme of the generated sensor. (B) Reflectance spectrum of the sensor for n_s = 1.332 and n_s = 1.337. (C) Dispersion curve of the sensor. (D) Plot of the real and imaginary part of the refractive index in the cross-section of the sensor. (E) Calculated distribution of the energy density of the optical field. (F) Map of reflectance as a function of wavelength and refractive index of the sensing layer shows the two modes.

Since each structure is a sequence of layers, the children were created in a similar fashion as in the algorithm for gene alignment.[40] Breeding uses both single-parent and two-parent operators—mutations and crossover. Mutations of single parents include the following:

- **Altering layer's thickness:** increases or decreases layer's thickness by a single thickness step size, fine-tuning the structure. If the resulting thickness falls outside of the set boundaries, the other option is chosen instead.
- **Changing layer's material:** switches layer's dieletric function for another one from the database
- **Switching two layers:** switches both thickness and dielectric function of two layers within a single parent
- **Adding a layer:** adds a new random layer to a random position
- **Deleting a layer:** deletes a random layer from the parent while at least one plasmonic metal needs to remain

Two-parent crossovers are realized either by

- **Crossover using a crossover point:** randomly chooses a crossover point for both parents, chooses which parts (before or after the crossover point) to switch and switches them between the parents
- **Switching two materials:** randomly chooses a layer from each parent and switches the materials

Again, each child must possess at least one plasmonic metal. The ratio of mutations and crossover is 33:67, and each child is a product of a single mutation or crossover. The mutation rate here is higher than commonly used,[39] which has been found to positively affect the speed of the algorithm.

Mutations and crossovers sometimes inevitably lead to the creation of structures that do not satisfy the aforementioned restricting conditions. Such structures are replaced by random structures from the pool of structures satisfying these conditions in order to ensure the diversity of the population. On the other hand, new structures that do satisfy these conditions are saved into the pool. This method of handling constraints helps mitigate the increase in runtime due to more complicated design targets or additional constraints, as the algorithm efficiently focuses on feasible solutions in the search space.

Figure 1B shows the evolution of the maximum sensitivity of each generation. It is apparent that the sensitivity does not increase linearly but rather follows a logarithmic function, quickly reaching a high value of sensitivity and then slowly converging to the optimal solution. Scatter plot of the

https://doi.org/10.1021/acsomega.3c01387
ACS Omega 2023, 8, 20792−20800

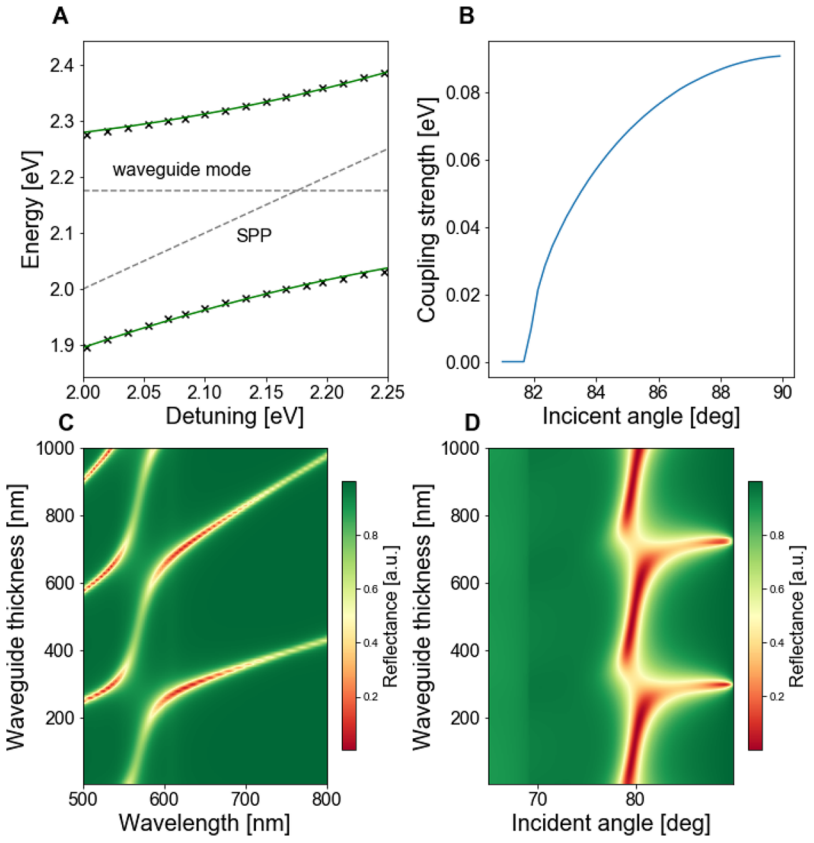

Figure 3. (A) Coupled mode oscillator fitting of E_+ and E_- branches of the system consisting of surface plasmon polariton and waveguide mode. Characteristic anticrossing is visible. (B) The coupling strength changes with the incident angle. (C) Map of different waveguide modes as a function of wavelength and waveguide thickness and (D) incident angle and waveguide thickness.

sensitivities of all populations shown in Figure 1C shows that in later generations, the majority of the population has a sensitivity around the maximum. Figure S1 shows a scheme that illustrates the evolution of the best structure in each generation, depicting the corresponding mutations and crossovers that have shaped the optimal designs over generations.

Dual-Mode SPR Sensor. We propose and explore an SPR sensor with multiple plasmonic modes, where the sensing is based on their intercoupling.

Such a structure is a result of the algorithm convergence without any additional restricting conditions and consists of a hybrid plasmonic waveguide structure with two plasmonic resonance modes. The dual-mode SPR sensor comprises a prism of "SUMITA FIR" glass with a refractive index of 1.425 at a wavelength of 633 nm, three layers of WS_2, 282 nm of GeO_2, and 47 nm of Ag (Figure 2A). There are two modes in the SPR structure that could switch to each other, resulting in potentially very large resonance angle change.

The angle-resolved reflectance spectrum in Figure 2B clearly shows that the dip can be deconvoluted into two different dips, while one of them is more pronounced than the other. With the refractive index change $\Delta n_s = 0.005$, the two dips switch, and the second one becomes more pronounced, which leads to the enormous change of the resonance angle of 6.78°, leading to an unprecedented sensitivity of 1364 deg/RIU. The map of the reflection as a function of incident angle and wavelength at Figure 2C shows that the SPP dispersion split into two branches with distinct frequencies.

Profile of the real and imaginary parts of the refractive index shown in Figure 4D may suggest that the A exciton absorption of WS_2 plays a major role in the splitting. The same structure without any WS_2 (Figure S2A) still features the mode splitting. That said, the WS_2 layer contributes to the nature of the modes nevertheless. With increasing the number of WS_2 layers, the absorption band of the A exciton in WS_2 starts to be more pronounced, coupling with the hybrid plasmonic-waveguide structure as shown in Figure S2B–G. Due to this complex interaction, the relationship between the number of WS_2 layers and the sensitivity of the SPR sensor is nontrivial, as shown in Figure S2H. The map of the energy density as a function of wavelength in Figure 2E at an excitation angle of 89° and n_s = 1.332 shows both modes. Changing n_s leads to energy redistribution between the two modes as shown in Figure S3; with n_s = 1.312, most energy is concentrated in the lower branch, and with n_s = 1.352, most energy is concentrated in the upper branch.

This behavior is explained by the coupling between the waveguide mode supported by the GeO_2 film and the plasmonic mode, which leads to the characteristic anticrossing when detuned by changing the refractive index as shown in Figure 2F.[41,42] We've analyzed the coupling of the two modes using a coupled oscillator model. The interaction between the waveguide mode and the plasmonic mode is described by the following equation:

$$\begin{pmatrix} E_{pl} - \frac{i\hbar\gamma_{pl}}{2} & g \\ g & E_{wg} - \frac{i\hbar\gamma_{wg}}{2} \end{pmatrix} \begin{pmatrix} \alpha \\ \beta \end{pmatrix} = E_{\pm} \begin{pmatrix} \alpha \\ \beta \end{pmatrix} \quad (1)$$

https://doi.org/10.1021/acsomega.3c01387
ACS Omega 2023, 8, 20792−20800

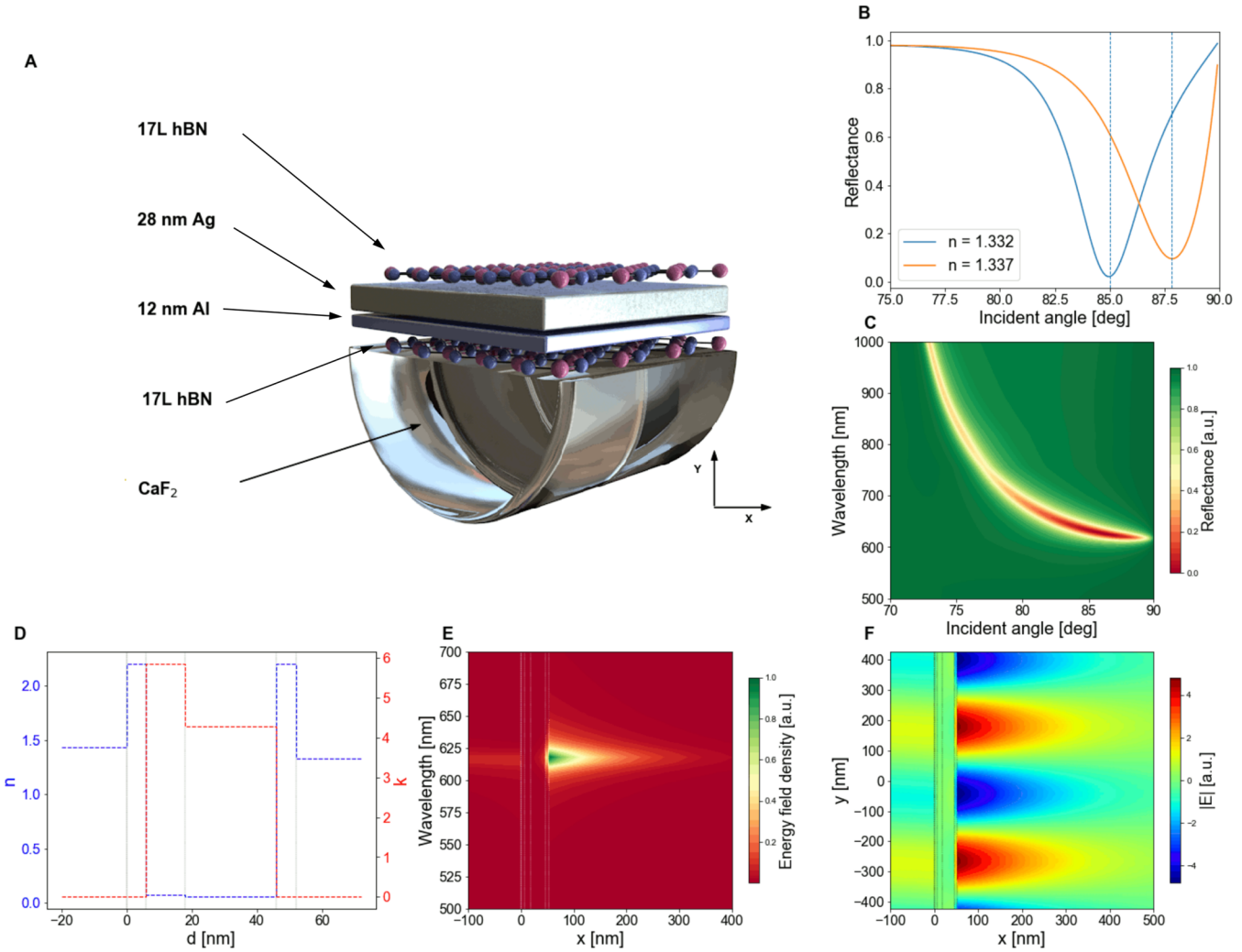

Figure 4. (A) Scheme of the optimized SPR sensor structure with the CaF2 coupling prism also shown. (B) Reflectance spectrum of the sensor for n_s = 1.332 and n_s = 1.337. (C) Dispersion curve of the sensor. (D) Plot of the real and imaginary part of the refractive index in the cross-section of the sensor. (E) Calculated distribution of the energy density of the optical field. (F) FDTD simulation of the vector of the electric field in the cross-section of the sensor.

where E_{pl} and E_{wg} are the frequencies of the surface plasmon polariton in the absence of the waveguide and of the waveguide mode, respectively. γ_{pl} and γ_{wg} are the dissipation rates of the two oscillators, g is the coupling strength, and $E_{\pm}$ are the eigenenergies of the new hybrid states. α and β are the eigenvector components called Hopfield coefficients and follow $|\alpha|^2 + |\beta|^2 = 1$. Solution of the eigenproblem gives rise to two energies:

$$E_{+} = (E_{wg} + E_{pl})/2 + \sqrt{(4g^2 + (E_{pl} - E_{wg} - i(\gamma_{pl} - \gamma_{wg})/2)^2} \quad (2)$$

$$E_{-} = (E_{wg} + E_{pl})/2 - \sqrt{(4g^2 + (E_{pl} - E_{wg} - i(\gamma_{pl} - \gamma_{wg})/2)^2} \quad (3)$$

Figure 3A shows the dispersion curves obtained by the coupled oscillator model fitted into the positions of the lower and upper branches obtained from Figure 2F. The coupling strength g obtained by the fitting is calculated as 88 meV. The dotted lines denote the energies of the waveguide and plasmonic modes, respectively.

In Figure 3B, we show how the coupling strength changes with the excitation angle. Therefore, this unique SPR structure is detuned by changing both the angle and the refractive index of the environment. This is analogous to previous studies of strong coupling with plasmonic nanoparticles and excitons within 2D materials, where the coupling strength is tunable by the refractive index environment,[42] nanoparticle dimension,[41] or electrostatic tuning of the 2D materials.[43] The fact that the coupling strength changes with the angle is not surprising and corresponds to the efficiency of the coupling between the incident light and the waveguide mode.

Altering the thickness of the GeO_2 has an impact on the mode supported by the waveguide. A thicker GeO_2 film leads to the redshift of the mode, and it only couples with the plasmonic mode at a frequency close to E_{SPP}. However, with increasing thickness, higher modes appear periodically and also couple to the surface plasmon polariton as shown in Figure 3C. Similarly, Figure 3D shows a map of reflectance as a function of incident angle and GeO_2 thickness and helps to understand the nature of the response.

Since the change of the resonance angle of our double-mode sensor is not linear, such a concept would be more useful for

https://doi.org/10.1021/acsomega.3c01387
ACS Omega 2023, 8, 20792−20800

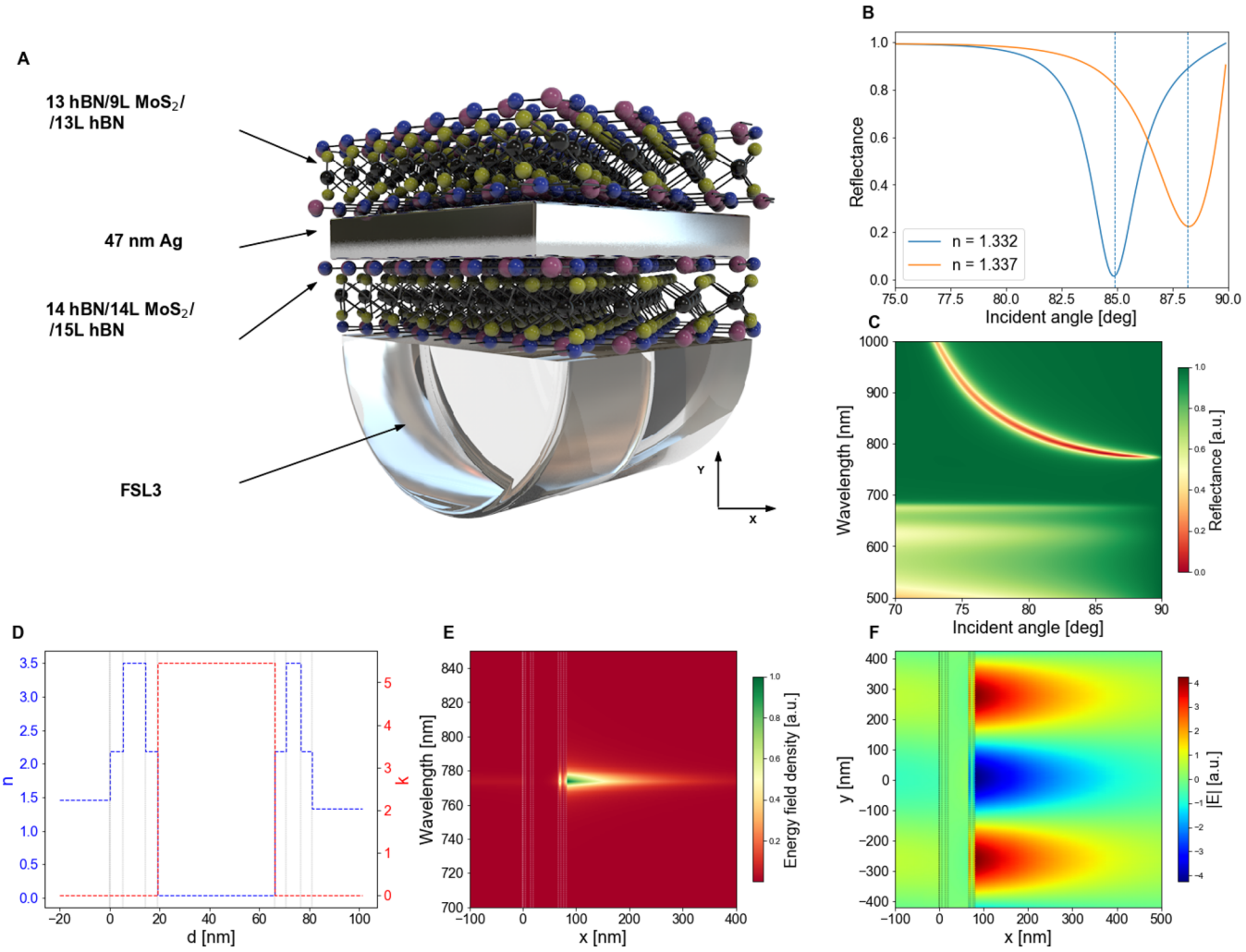

Figure 5. (A) Scheme of the generated sensor. (B) Reflectance spectrum of the sensor for $n_2 = 1.332$ and $n_2 = 1.337$. (C) Dispersion curve of the sensor. (D) Plot of the real and imaginary part of the refractive index in the cross-section of the sensor. (E) Calculated distribution of the energy density of the optical field. (F) FDTD simulation of the vector of the electric field in the cross-section of the sensor.

qualitative analysis as a sensor with a threshold. Furthermore, the nonlinear response of a plasmonic device might find applications beyond biosensors such as an optical plasmonic switch,[44] especially when combined with tunable optical materials such as GST,[45] WS_2,[46] or BST.[47] The tunability of WS_2 might also be employed as an inherent property of the double-mode sensor to fine-tune the overlap of the plasmonic mode with the waveguide mode and thus make the fabrication easier. While we acknowledge that the high angle of the incident light complicates practical implementation due to the possible walk-off of the beam, recent progress in wide-angle meta-optics helps to overcome the limitations.[48,49]

The design of this SPR sensor took around 2 h on a personal computer with an Intel i5−8250U CPU without utilizing GPU parallelization.

Optimization SPR Sensors at 633 nm. For optimization of the conventional SPR structure with a single mode, we've chosen certain restrictive boundaries. To obtain a clean plasmonic resonance dip with a single mode, we've analyzed all the dips in the spectra and calculated their first and second derivatives at the local minima, the symmetry calculated from the aforementioned fwhm, and the depth of the dip. The symmetry, which is defined as a ratio of the left and right halves of the dip, was limited to 1.25. Furthermore, the dip needs to be deeper than 40% to prevent the algorithm from returning structures with dips difficult to measure with standard optical techniques, and the dip needs to be smooth, which is ensured by limiting the number of peaks in the first and second derivatives of the function. In case there is more than one dip in the spectra, we perform a peak tracing by simply comparing the ratios of the first derivatives of the dips in structures with the basic and altered refractive indices of the sensing layer and then matching the respective peaks.

The optimized structure, which is shown in Figure 4A, has a bimetallic architecture and consists of a CaF_2 prism ($n = 1.43$), 17 layers of hexagonal boron nitride (hBN), 12 nm of Al, 28 nm of Ag, and another protecting layer of hBN. Such a structure is relatively easy to fabricate since it is possible to deposit a large-scale hBN with CVD[50] and does not require the use of any exotic materials or materials difficult to deposit.

The sensor has a theoretical sensitivity of 578 deg/RIU, which means that changing the refractive index of the sensing layer by 0.005 yields an angular shift of 2.89° as shown in Figure 4B. The output from the genetic algorithm is an already optimized structure, and further optimization by altering the thicknesses of particular layers does not lead to any

https://doi.org/10.1021/acsomega.3c01387
ACS Omega 2023, 8, 20792−20800

improvement of the sensitivity. The achieved sensitivity of 578 deg/RIU in this structure is 262% higher than that of an SPR sensor with a single Ag metal layer (Figure S4) and 8% higher than that of the ultrasensitive structure we previously reported.[22] Furthermore, there is no need for an air-gap layer, as in ref 22, which will make the sensor fabrication much easier.

The high sensitivity of the sensor can be understood from the dispersion curve in Figure 4C. The sensitivity highly depends on the slope of the dispersion curve.[51] As the sensor operates near the effective plasma frequency,[52] the slope of the dispersion curve is very small, which translates into a high angular shift.

The dispersion curve is primarily determined by the bimetallic Al/Ag system. Switching the two metals or replacing one with another leads to dramatic changes in the nature of the dispersion curve. The two hBN layers fine-tune the dispersion curve and at the same time protect the metal surface as hBN is a viable alternative for commonly used graphene protectors.[53] Changing the thickness of the hBN layer on top of the Ag layer leads to a dramatic shift of the dispersion curve, while altering the hBN layer between the prism and Al leads to a modest change in dispersion and the depth of the dip, indicating that the middle hBN layer facilitates interaction between the two metals.

Figure 4D illustrates the profile of real and complex parts of the refractive index across the layered structure, and Figure 4E displays the distribution of the energy density of the optical field (the length of the Poynting vector |S|) throughout the SPR structure in the layered thickness direction as a function of the wavelength. The zero position is set at the prism interface. The enhancement at the interface of the metal and the sensing layer is shown clearly. Similarly, the finite difference time domain (FDTD) simulation in Figure 4F of the electric field profile on the interface shows the propagation of the surface plasmon polariton along with the interface and a uniform extension of the electric field into the sensing layer.

Optimization of SPR Sensors at 785 nm. Besides optimizing the SPR sensor for the most used wavelength of 633 nm, we have also performed an optimization for a near-IR wavelength of 785 nm, which is readily available from fiber-coupled near-IR diode lasers, to validate the robustness of the algorithm and to check the possible SPR sensitivity. Moreover, longer wavelengths allow for a measurement of a thicker sensing layer.[54] This structure has more 2D materials included, as shown in Figure 5A, and yields a sensitivity of 676.4 RIU/deg, which is significantly higher than that of the sensor operating in the visible range. It consists of a fluorosilicate prism (OHARA FSL3; $n = 1.46$), 15 layers of hBN, 14 layers of MoS_2, 14 layers of hBN, 47 nm of Ag, and nine layers of MoS_2 sandwiched between seven layers of hBN. The sensitivity is 528% higher than that of a structure consisting only of a prism with 47 nm of Ag (Figure S4).

The SPP dispersion at Figure 5C shows that, compared to the previous case, the plasmon dispersion is red-shifted, and the dispersion is flatter in the region near the effective plasma frequency, which explains the higher sensitivity. As shown in Figure 5D, MoS_2 is practically lossless at this wavelength, unlike in the visible range, which manifests in the absorption pattern visible in the lower part of Figure 5C. The MoS_2 together with hBN here fine-tune the dispersion. The layers separating the silver and the sensing layer have a dramatic effect on the effective plasma frequency, while the layers separating the prism and the silver layer slightly flatten the dispersion curve. As seen in Figure 5E, the energy density of the plasmonic resonance is higher for this sensor than in the previous case, and the resonance is sharper.

FDTD simulation of the E_x profile in Figure 5F at the plasmonic resonance reveals the surface plasmon resonance to be 24% longer, which is consistent with the change of the excitation wavelength.

DISCUSSION AND CONCLUSION

The presented method significantly reduces the time needed for the design of SPR sensors and multilayer photonic systems in general. Figure S5 in the manuscript demonstrates the evolution of maximum sensitivity in different generations for both conventional SPR and the dual-mode sensor. While the conventional SPR converges after less than 10 generations, it takes around 90 generations for the dual-mode sensor to converge. The runtime of the dual-mode optimization is approximately 2 h, whereas the conventional SPR takes less than 1 h. It is important to note that our implementation of the transfer TMM includes full magneto-optic tensors allowing a generalization of the problem, which increases the runtime,[33] and when switching to a simpler formula for the TMM calculation,[22] the runtime of the algorithm is reduced to mere minutes. Moreover, the GA approach is parallelizable, which can further speed up the process and decrease computational complexity.[55] This offers a significant advantage not only compared to the *ad hoc* design of multilayer SPR sensors but also compared to a potential use of other optimization and inverse design methods. Compared to gradient-based optimization methods like L-BFGS and the conjugate gradient, and global optimization techniques such as particle swarm optimization (PSO) and simulated annealing (SA), GAs efficiently explore the solution space, often converging faster to optimal or near-optimal solutions, even in complex design problems.[56] GAs demonstrate robustness against premature convergence[57] and effectiveness in nonlinear, discontinuous, and multimodal optimization problems.[58] In comparison to deep learning methods, which have gained popularity in recent years, GAs do not require large amounts of training data or high computational resources, making them a more practical choice for optimizing multilayer photonic structures. Additionally, deep learning methods can be more challenging to interpret and understand, whereas GAs offer a more transparent and intuitive approach to problem-solving in this context.[59,60]

In conclusion, we've successfully demonstrated the optimization of SPR sensors based on a multilayer photonic system and a significant improvement of the sensitivity compared to a system comprising only a prism and a single plasmonic layer. The employed algorithm features sufficient robustness and variability to be implemented for various cases of tailored SPR sensors. Furthermore, we've demonstrated a novel concept of a tunable SPR sensor with a coupled waveguide-plasmonic mode with a sensitivity of 1364 deg/RIU and provided examples of ultrasensitive single-mode SPR sensors for an excitation wavelength of 633 nm with a sensitivity of 578 deg/RIU and a near-infrared wavelength of 785 nm with a sensitivity of 676 deg/RIU.

https://doi.org/10.1021/acsomega.3c01387
ACS Omega 2023, 8, 20792−20800

METHODS

Transfer Matrix Method. The transfer matrix method is used in a generalized form with 2 × 2 matrices accounting for the initial polarization of incident light and using a general dielectric tensor ϵ_{ij} allowing for the full calculations of E and H vectors. The full details of the calculation are thoroughly described elsewhere.[33,61]

Finite Difference Time Domain. All FDTD simulations were done with Lumerical using Perfect Matching layer boundary conditions[62] in the direction perpendicular to the multilayer system and Bloch boundary conditions in the parallel direction. Refractive indices were the same as in the case of TMM, and a plane wave of a single frequency was used as an excitation source.

ASSOCIATED CONTENT

Supporting Information

The Supporting Information is available free of charge at https://pubs.acs.org/doi/10.1021/acsomega.3c01387.

List of dielectric constants used in the study, reference reflectance spectra of a sensor with a single 47 nm layer of Ag, dispersion curves of the dual-mode sensor varying the number of layers of WS_2, energy field density maps of the dual-mode sensors varying n_s, evolution of the single mode 633 nm strcuture with the highest enhnacement for different generations (PDF)

AUTHOR INFORMATION

Corresponding Authors

Matej Sebek − *Biophysics Group, Department of Physics and Astronomy, University College London, London WC1E 6BT, United Kingdom; UCL Healthcare Biomagnetics and Nanomaterials Laboratories, London W1S 4BS, United Kingdom; Institute of Materials Research and Engineering, Innovis, Singapore 138634;* orcid.org/0000-0002-5196-6951; Email: matej.sebek.17@ucl.ac.uk

Jinghua Teng − *Institute of Materials Research and Engineering, Innovis, Singapore 138634;* orcid.org/0000-0001-5331-3092; Email: jh-teng@imre.a-star.edu.sg

Authors

Nguyen Thi Kim Thanh − *Biophysics Group, Department of Physics and Astronomy, University College London, London WC1E 6BT, United Kingdom; UCL Healthcare Biomagnetics and Nanomaterials Laboratories, London W1S 4BS, United Kingdom;* orcid.org/0000-0002-4131-5952

Xiaodi Su − *Institute of Materials Research and Engineering, Innovis, Singapore 138634;* orcid.org/0000-0003-2164-4588

Complete contact information is available at: https://pubs.acs.org/10.1021/acsomega.3c01387

Notes

The authors declare no competing financial interest.

ACKNOWLEDGMENTS

The work is partially supported by the Agency for Science, Technology and Research (A*STAR) under Grants of IAF-PP H19H6a0025, IRG Grant A20E5c0084 and Pharos Programme 1527000014, and ARAP program.

REFERENCES

(1) Sebek, M.; Elbana, A.; Nemati, A.; Pan, J.; Shen, Z. X.; Hong, M.; Su, X.; Thanh, N. T. K.; Teng, J. Hybrid Plasmonics and Two-Dimensional Materials: Theory and Applications. *Journal of Molecular and Engineering Materials* **2020**, *8*, 2030001.

(2) Zhao, M.; Li, J.; Sebek, M.; Yang, L.; Liu, Y. J.; Bosman, M.; Wang, Q.; Zheng, X.; Lu, J.; Teng, J. Electrostatically Tunable Near-Infrared Plasmonic Resonances in Solution-Processed Atomically Thin NbSe2. *Adv. Mater.* **2021**, *33*, 2101950.

(3) Xu, T.; Wu, Y.-K.; Luo, X.; Guo, L. J. Plasmonic nanoresonators for high-resolution colour filtering and spectral imaging. *Nat. Commun.* **2010**, *1*, 1−5.

(4) Demir Duman, F.; Sebek, M.; Thanh, N. T. K.; Loizidou, M.; Shakib, K.; MacRobert, A. J. Enhanced photodynamic therapy and fluorescence imaging using gold nanorods for porphyrin delivery in a novel in vitro squamous cell carcinoma 3D model. *J. Mater. Chem. B* **2020**, *8*, 5131−5142.

(5) Mejía-Salazar, J.; Oliveira, O. N., Jr Plasmonic biosensing: focus review. *Chem. Rev.* **2018**, *118*, 10617−10625.

(6) Ma, R.-M.; Oulton, R. F. Applications of nanolasers. *Nature Nanotechnol.* **2019**, *14*, 12−22.

(7) Kristensen, A.; Yang, J. K.; Bozhevolnyi, S. I.; Link, S.; Nordlander, P.; Halas, N. J.; Mortensen, N. A. Plasmonic colour generation. *Nature Reviews Materials* **2017**, *2*, 1−14.

(8) Homola, J.; Yee, S. S.; Gauglitz, G. Surface plasmon resonance sensors. *Sens. Actuators, B* **1999**, *54*, 3−15.

(9) Liedberg, B.; Nylander, C.; Lunström, I. Surface plasmon resonance for gas detection and biosensing. *Sensors and actuators* **1983**, *4*, 299−304.

(10) Qiu, G.; Gai, Z.; Tao, Y.; Schmitt, J.; Kullak-Ublick, G. A.; Wang, J. Dual-functional plasmonic photothermal biosensors for highly accurate severe acute respiratory syndrome coronavirus 2 detection. *ACS Nano* **2020**, *14*, 5268.

(11) Homola, J. Surface plasmon resonance sensors for detection of chemical and biological species. *Chem. Rev.* **2008**, *108*, 462−493.

(12) Lahav, A.; Auslender, M.; Abdulhalim, I. Sensitivity enhancement of guided-wave surface-plasmon resonance sensors. *Opt. Lett.* **2008**, *33*, 2539−2541.

(13) Cai, D.; Lu, Y.; Lin, K.; Wang, P.; Ming, H. Improving the sensitivity of SPR sensors based on gratings by double-dips method (DDM). *Opt. Express* **2008**, *16*, 14597−14602.

(14) Yuan, J.; Oliver, R.; Li, J.; Lee, J.; Aguilar, M.; Wu, Y. Sensitivity enhancement of SPR assay of progesterone based on mixed self-assembled monolayers using nanogold particles. *Biosens. Bioelectron.* **2007**, *23*, 144−148.

(15) Blanchard-Dionne, A.; Guyot, L.; Patskovsky, S.; Gordon, R.; Meunier, M. Intensity based surface plasmon resonance sensor using a nanohole rectangular array. *Opt. Express* **2011**, *19*, 15041−15046.

(16) Lahav, A.; Shalabaney, A.; Abdulhalim, I. S. Surface plasmon sensor with enhanced sensitivity using top nano dielectric layer. *Journal of Nanophotonics* **2009**, *3*, 031501.

(17) Wu, L.; Chu, H.; Koh, W.; Li, E. Highly sensitive graphene biosensors based on surface plasmon resonance. *Opt. Express* **2010**, *18*, 14395−14400.

(18) Ouyang, Q.; Zeng, S.; Jiang, L.; Hong, L.; Xu, G.; Dinh, X.-Q.; Qian, J.; He, S.; Qu, J.; Coquet, P.; Yong, K.-T.; et al. Sensitivity enhancement of transition metal dichalcogenides/silicon nanostructure-based surface plasmon resonance biosensor. *Sci. Rep.* **2016**, *6*, 28190.

(19) Wu, L.; Guo, J.; Wang, Q.; Lu, S.; Dai, X.; Xiang, Y.; Fan, D. Sensitivity enhancement by using few-layer black phosphorus-graphene/TMDCs heterostructure in surface plasmon resonance biochemical sensor. *Sens. Actuators, B* **2017**, *249*, 542−548.

(20) Dai, X.; Liang, Y.; Zhao, Y.; Gan, S.; Jia, Y.; Xiang, Y. Sensitivity Enhancement of a Surface Plasmon Resonance with Tin Selenide (SnSe) Allotropes. *Sensors* **2019**, *19*, 173.

(21) Ouyang, Q.; Zeng, S.; Jiang, L.; Qu, J.; Dinh, X.-Q.; Qian, J.; He, S.; Coquet, P.; Yong, K.-T. Two-dimensional transition metal

https://doi.org/10.1021/acsomega.3c01387
ACS Omega 2023, 8, 20792−20800

dichalcogenide enhanced phase-sensitive plasmonic biosensors: Theoretical insight. *J. Phys. Chem. C* **2017**, *121*, 6282−6289.
(22) Feng, Y.; Liu, Y.; Teng, J. Design of an ultrasensitive SPR biosensor based on a graphene-MoS 2 hybrid structure with a MgF 2 prism. *Applied optics* **2018**, *57*, 3639−3644.
(23) Weile, D. S.; Michielssen, E. Genetic algorithm optimization applied to electromagnetics: A review. *IEEE Transactions on Antennas and Propagation* **1997**, *45*, 343−353.
(24) Shen, L.; Ye, Z.; He, S. Design of two-dimensional photonic crystals with large absolute band gaps using a genetic algorithm. *Phys. Rev. B* **2003**, *68*, 035109.
(25) Preble, S.; Lipson, M.; Lipson, H. Two-dimensional photonic crystals designed by evolutionary algorithms. *Appl. Phys. Lett.* **2005**, *86*, 061111.
(26) Kerrinckx, E.; Bigot, L.; Douay, M.; Quiquempois, Y. Photonic crystal fiber design by means of a genetic algorithm. *Opt. Express* **2004**, *12*, 1990−1995.
(27) Forestiere, C.; Pasquale, A. J.; Capretti, A.; Miano, G.; Tamburrino, A.; Lee, S. Y.; Reinhard, B. M.; Dal Negro, L. Genetically engineered plasmonic nanoarrays. *Nano Lett.* **2012**, *12*, 2037−2044.
(28) Mahani, F.; Mahanipour, A.; Mokhtari, A. Optimization of plasmonic color filters for CMOS image sensors by genetic algorithm. *2017 2nd Conference on Swarm Intelligence and Evolutionary Computation (CSIEC)*, March 7−9, 2017; IEEE, 2017; pp 12−15.
(29) Liang, H.; Lin, Q.; Xie, X.; Sun, Q.; Wang, Y.; Zhou, L.; Liu, L.; Yu, X.; Zhou, J.; Krauss, T. F.; et al. Ultrahigh numerical aperture metalens at visible wavelengths. *Nano Lett.* **2018**, *18*, 4460−4466.
(30) Jafar-Zanjani, S.; Inampudi, S.; Mosallaei, H. Adaptive genetic algorithm for optical metasurfaces design. *Sci. Rep.* **2018**, *8*, 1−16.
(31) Bahrami, F.; Maisonneuve, M.; Meunier, M.; Aitchison, J. S.; Mojahedi, M. An improved refractive index sensor based on genetic optimization of plasmon waveguide resonance. *Opt. Express* **2013**, *21*, 20863−20872.
(32) Lin, C.; Chen, S. Design of highly sensitive guided-wave surface plasmon resonance biosensor with deep dip using genetic algorithm. *Opt. Commun.* **2019**, *445*, 155−160.
(33) Pellegrini, G.; Mattei, G. High-performance magneto-optic surface plasmon resonance sensor design: An optimization approach. *Plasmonics* **2014**, *9*, 1457−1462.
(34) Lin, C.; Chen, S. Design of high-performance Au-Ag-dielectric-graphene based surface plasmon resonance biosensors using genetic algorithm. *J. Appl. Phys.* **2019**, *125*, 113101.
(35) Xia, G.; Zhou, C.; Jin, S.; Huang, C.; Xing, J.; Liu, Z. Sensitivity enhancement of two-dimensional materials based on genetic optimization in surface plasmon resonance. *Sensors* **2019**, *19*, 1198.
(36) Fu, P.-H.; Lo, S.-C.; Tsai, P.-C.; Lee, K.-L.; Wei, P.-K. Optimization for gold nanostructure-based surface plasmon biosensors using a microgenetic algorithm. *ACS Photonics* **2018**, *5*, 2320−2327.
(37) Kretschmann, E.; Raether, H. Radiative decay of non radiative surface plasmons excited by light. *Zeitschrift für Naturforschung A* **1968**, *23*, 2135−2136.
(38) Polyanskiy, M. N. Refractive index database. https://refractiveindex.info (accessed on July 2, 2021).
(39) Hassanat, A.; Almohammadi, K.; Alkafaween, E.; Abunawas, E.; Hammouri, A.; Prasath, V. S. Choosing mutation and crossover ratios for genetic algorithms—a review with a new dynamic approach. *Information* **2019**, *10*, 390.
(40) Notredame, C.; Higgins, D. G. SAGA: sequence alignment by genetic algorithm. *Nucleic acids research* **1996**, *24*, 1515−1524.
(41) Wen, J.; Wang, H.; Wang, W.; Deng, Z.; Zhuang, C.; Zhang, Y.; Liu, F.; She, J.; Chen, J.; Chen, H.; et al. Room-temperature strong light−matter interaction with active control in single plasmonic nanorod coupled with two-dimensional atomic crystals. *Nano Lett.* **2017**, *17*, 4689−4697.
(42) Zheng, D.; Zhang, S.; Deng, Q.; Kang, M.; Nordlander, P.; Xu, H. Manipulating coherent plasmon−exciton interaction in a single silver nanorod on monolayer WSe2. *Nano Lett.* **2017**, *17*, 3809−3814.
(43) Munkhbat, B.; Baranov, D. G.; Bisht, A.; Hoque, M. A.; Karpiak, B.; Dash, S. P.; Shegai, T. Electrical control of hybrid monolayer tungsten disulfide−plasmonic nanoantenna light−matter states at cryogenic and room temperatures. *ACS Nano* **2020**, *14*, 1196−1206.
(44) Sun, Y.; Jiang, L.; Zhong, L.; Jiang, Y.; Chen, X. Towards active plasmonic response devices. *Nano Research* **2015**, *8*, 406−417.
(45) Wang, Q.; Rogers, E. T.; Gholipour, B.; Wang, C.-M.; Yuan, G.; Teng, J.; Zheludev, N. I. Optically reconfigurable metasurfaces and photonic devices based on phase change materials. *Nat. Photonics* **2016**, *10*, 60−65.
(46) Yu, Y.; Yu, Y.; Huang, L.; Peng, H.; Xiong, L.; Cao, L. Giant gating tunability of optical refractive index in transition metal dichalcogenide monolayers. *Nano Lett.* **2017**, *17*, 3613−3618.
(47) Nemati, A.; Wang, Q.; Ang, N. S. S.; Wang, W.; Hong, M.; Teng, J. Ultra-high extinction-ratio light modulation by electrically tunable metasurface using dual epsilon-near-zero resonances. *Opto-Electronic Advances* **2021**, *4*, 200088−1.
(48) Spägele, C.; Tamagnone, M.; Kazakov, D.; Ossiander, M.; Piccardo, M.; Capasso, F. Multifunctional wide-angle optics and lasing based on supercell metasurfaces. *Nat. Commun.* **2021**, *12*, 1−10.
(49) Lin, D.; Melli, M.; Poliakov, E.; Hilaire, P. S.; Dhuey, S.; Peroz, C.; Cabrini, S.; Brongersma, M.; Klug, M. Optical metasurfaces for high angle steering at visible wavelengths. *Sci. Rep.* **2017**, *7*, 1−8.
(50) Kim, K. K.; Hsu, A.; Jia, X.; Kim, S. M.; Shi, Y.; Hofmann, M.; Nezich, D.; Rodriguez-Nieva, J. F.; Dresselhaus, M.; Palacios, T.; et al. Synthesis of monolayer hexagonal boron nitride on Cu foil using chemical vapor deposition. *Nano Lett.* **2012**, *12*, 161−166.
(51) El-Gohary, S. H.; Eom, S.; Lee, S. Y.; Byun, K. M. Dispersion curve-based sensitivity engineering for enhanced surface plasmon resonance detection. *Opt. Commun.* **2016**, *370*, 299−305.
(52) Xu, X.; Xi, Y.; Han, D.; Liu, X.; Zi, J.; Zhu, Z. Effective plasma frequency in one-dimensional metallic-dielectric photonic crystals. *Appl. Phys. Lett.* **2005**, *86*, 091112.
(53) Wu, F.; Thomas, P. A.; Kravets, V. G.; Arola, H. O.; Soikkeli, M.; Iljin, K.; Kim, G.; Kim, M.; Shin, H. S.; Andreeva, D. V.; Neumann, C.; Kullmer, M.; Turchanin, A.; De Fazio, D.; Balci, O.; Babenko, V.; Luo, B.; Goykhman, I.; Hofmann, S.; Ferrari, A. C.; Novoselov, K. S.; Grigorenko, A. N. Layered material platform for surface plasmon resonance biosensing. *Sci. Rep.* **2019**, *9*, 1−10.
(54) Lakayan, D.; Tuppurainen, J.; Albers, M.; van Lint, M. J.; van Iperen, D. J.; Weda, J. J.; Kuncova-Kallio, J.; Somsen, G. W.; Kool, J. Angular scanning and variable wavelength surface plasmon resonance allowing free sensor surface selection for optimum material-and biosensing. *Sens. Actuators, B* **2018**, *259*, 972−979.
(55) Cantu-Paz, E. *Efficient and Accurate Parallel Genetic Algorithms*; Springer Science & Business Media, 2000; Vol. *1*.
(56) Goldberg, D. E. *Genetic Algorithmin in Search. Optimization and Machine Learning*; Addison-Wesley Professional, 1989.
(57) Mitchell, M. *An Introduction to Genetic Algorithms*; MIT Press, 1998.
(58) Deb, K. *Multi-Objective Optimization Using Evolutionary Algorithms: an Introduction*; Springer, 2011.
(59) Peurifoy, J.; Shen, Y.; Jing, L.; Yang, Y.; Cano-Renteria, F.; DeLacy, B. G.; Joannopoulos, J. D.; Tegmark, M.; Soljačić, M. Nanophotonic particle simulation and inverse design using artificial neural networks. *Science Adv.* **2018**, *4*, No. eaar4206.
(60) Wiecha, P. R.; Arbouet, A.; Girard, C.; Muskens, O. L. Deep learning in nano-photonics: inverse design and beyond. *Photonics Research* **2021**, *9*, B182−B200.
(61) Mansuripur, M. Analysis of multilayer thin-film structures containing magneto-optic and anisotropic media at oblique incidence using 2× 2 matrices. *J. Appl. Phys.* **1990**, *67*, 6466−6475.
(62) Bérenger, J.-P. *Perfectly Matched Layer (PML) for Computational Electromagnetics*; Synthesis Lectures on Computational Electromagnetics; Springer International Publishing: Cham, 2007; vol *2*, pp 1−117.

https://doi.org/10.1021/acsomega.3c01387
ACS Omega 2023, 8, 20792−20800